

Low Latency Instance Segmentation by Continuous Clustering for Rotating LiDAR Sensors

Andreas Reich and Hans-Joachim Wuensche

Abstract—Low-latency instance segmentation of LiDAR point clouds is crucial in real-world applications because it serves as an initial and frequently-used building block in a robot’s perception pipeline, where every task adds further delay. Particularly in dynamic environments, this total delay can result in significant positional offsets of dynamic objects, as seen in highway scenarios. To address this issue, we employ continuous clustering of obstacle points in order to obtain an instance-segmented point cloud. Unlike most existing approaches, which use a full revolution of the LiDAR sensor, we process the data stream in a continuous and seamless fashion. More specifically, each column of a range image is processed as soon it is available. Obstacle points are clustered to existing instances in real-time and it is checked at a high-frequency whether instances are completed and are ready to be published. An additional advantage is that no problematic discontinuities between the points of the start and the end of a scan are observed. In this work we describe the two-layered data structure and the corresponding algorithm for continuous clustering, which is able to cluster the incoming data in real time. We explain the importance of a large perceptive field of view. Furthermore, we describe and evaluate important architectural design choices, which could be relevant to design an architecture for deep learning based low-latency instance segmentation. We are publishing the source code at https://github.com/UniBwTAS/continuous_clustering.

I. INTRODUCTION

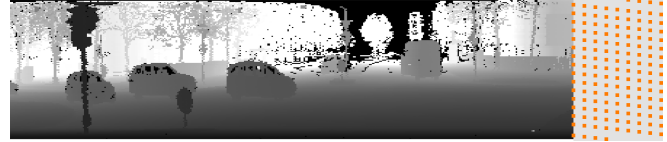
Instance segmentation for LiDAR points is crucial in robotics, as it enables the precise recognition and differentiation of objects in 3D space, facilitating safer and more efficient navigation and interaction with the environment. The resulting instances can be processed in downstream perception tasks, such as multi-object tracking based on the tracking-by-detection framework or landmark-based simultaneous localization and mapping (SLAM).

A simple but effective and verifiable approach for instance segmentation is Euclidean distance based clustering of LiDAR points. Thus, any two points are clustered if their mutual distance is below a threshold d_T . Another major advantage is that it can detect any type of object class unlike typical supervised learning-based instance segmentation approaches, which are trained to recognize a predefined set of object classes.

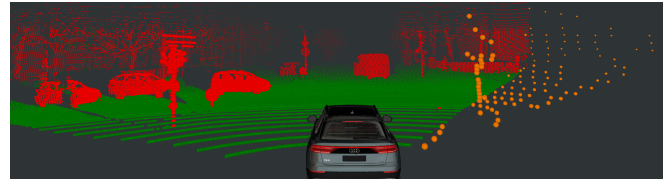
We extend this concept to continuous clustering as visualized in Figure 1. This means that the algorithm does not only start after a full rotation of the LiDAR sensor, but

The authors gratefully acknowledge funding by the Federal Office of Bundeswehr Equipment, Information Technology and In-Service Support (BAAINBw).

Both authors are with Institute for Autonomous Systems Technology (TAS), University of the Bundeswehr Munich, Neubiberg, Germany andreas.reich@unibw.de



(a) Extract of infinite range image with single firing (orange)



(b) Online ground point classification with single firing (orange)



(c) Clustering output (published as soon as all lasers have passed)

Fig. 1: Continuous clustering: (a) An infinite range image is constructed from a continuous stream of firings (a single shot from all laser diodes). Each point within a firing has a specific constant azimuth offset in order to reduce interference between laser beams. (b) Once a column in the range image is complete (rearmost laser of firing has passed the column), the points are classified as ground (green) and obstacle points (red). (c) The obstacle points are clustered if their mutual distance is below a threshold d_T and published as soon as no more points can be added (rearmost laser is distant enough).

directly starts extracting individual instances as soon as they are complete.

When designing our algorithm we keep the following three goals in mind: First, we want to be able to handle the stream of data in real time even for modern high-resolution sensors with a large number of points. We use the Velodyne VLS 128 LiDAR sensor with 128 lasers. The concepts, however, can be transferred to other rotational LiDAR sensors. Second, we still want to be able to use a large field of view (FOV) in order to also handle difficult scenarios, where an object is bisected by a closer object, such as a pole. Third, we design the algorithm to run on CPU in order to free the GPU resources for deep learning based perception tasks, like object detection in camera images.

We provide a short video¹ illustrating the capability of our method.

II. RELATED WORK

To the best of our knowledge, there is currently no approach capable of seamlessly integrating the continuously incoming points from a LiDAR sensor into a continuous data and object representation without intermediate accumulation. While in classical distance-based clustering it is common to accumulate an entire rotation of the sensor, there are several machine learning techniques capable of processing slices of a rotation [1]–[4]. Our work builds upon the concepts of existing distance-based clustering approaches on range images. Therefore, these will be discussed in detail in order to explain and motivate the design choices of our algorithm.

a) Range Image Generation: Almost all methods use the metadata and the ordered data stream to sort the points into a range image, where rows correspond to individual lasers sorted by elevation angle, and columns contain points with similar azimuth angles [5]–[10]. Compared to spherical projection based methods [11], this leads to a compact but complete data representation. Therefore, in our approach the continuous range image is also generated by extending the concepts of this method.

The range image is typically represented by a graph, with pixels corresponding to the nodes and edges representing direct neighborhoods. This generalized data structure can also represent the cyclical nature of the range image or missing measurements. Moreover, the graph is ideally suited for subsequent algorithms as edges can be removed if the Euclidean distance between two cells is too large. Likewise, edges that go beyond direct neighborhoods can be added to cluster across missing measurements or occlusions.

b) Ground Point Segmentation: In the next step, most approaches carry out a ground point segmentation [6]–[11]. This is especially crucial for purely distance-based clustering; otherwise, all objects would be merged across the ground plane. Only [5] forgoes this segmentation, treating the ground points as a separate cluster. This, however, requires an adjusted metric in the subsequent stage to prevent generating edges between ground and obstacle points. Our approach also removes the ground points in order to reduce the work load and the complexity in subsequent steps.

c) Conditions for Edge Generation: In the next step, edges are inserted or deleted between the remaining nodes. There are purely Euclidean distance-based approaches [7], [10], [11] and those that introduce additional conditions [5], [6], [8], [9]. For example [5] additionally requires a sharp increase between vertically adjacent points to ensure that there is no edge between the ground and obstacle points. As another condition, convexity is often taken into account [5], [6], [9]. The goal is to be able to separate even two spatially close objects. For instance, the bodies of two people walking side by side, when viewed in a laser ring from a bird’s-eye perspective, roughly represent two semi-circles in

close proximity. However, the points between them are not arranged convexly, so the edge in the graph is removed at this point. While these conditions are combined using an AND operation, [8] introduces a different condition for horizontal edges, which is combined with the distance condition using an OR operation. Here, even if the distance between directly adjacent points is too large, an edge is maintained when the current point and its two horizontal neighbors lie approximately on a straight line. The idea is that at large distances or at steep angles of incidence on a plane, the points are sparsely distributed even though they belong to the same object. An example of this would be distant points on the walls of a long tunnel. Our approach is also exclusively distance-based in order to keep the explanations simple. Nevertheless, we can readily extend our method to accommodate additional conditions.

d) Hierarchical Clustering: In the final step, all approaches commonly aim to identify the resulting connected components, which are subgraphs that aren’t part of a larger graph. This is a well-known problem in graph theory and is typically referred to as connected component labeling (CCL). The usual approach iterates over all yet unvisited nodes, which then serve as the starting point for a traversal method, e.g. Breadth-First-Search (BFS). In each run of the traversal method, all nodes are assigned the same label as the starting node and marked as visited.

In order to increase the perceptive field of view and to make this last step more efficient, which is primarily dependent on the sum of the number of nodes and edges, many newer approaches aggregate nodes of the graph into super nodes during graph construction [7]–[11]. This is done hierarchically, by first clustering the points in one dimension of the depth image, i.e., row- or column-wise. These clusters form the super nodes in a new graph. To add the remaining edges in this new graph, the resulting super nodes are then compared in the second dimension.

The first dimension can be processed quickly and is typically parallelized. This allows for considering neighbors beyond the direct vicinity, which is essential, for instance, to bridge occlusions. While some approaches only consider the immediate neighborhood and merely skip invalid points [7], [9], [10], others use a larger one dimensional perceptive field of view [8], [11].

The process of finding remaining edges by evaluating the second dimension is considerably more computation-intensive since, for formal correctness, every cluster would theoretically have to be compared with every other. In practice, the current cluster is usually only compared with clusters in the previous row (or column). When comparing two clusters, in the worst-case scenario, each point of one cluster must be compared with each point of the other to identify the existence of a desired condition, e.g. falling below a distance threshold, in at least one pair [9]. Once such a pair is found, the comparison of two clusters can be stopped, and an edge is created. Even when only considering the previous row or column, combinatorics leads to many pairwise point comparisons, so it’s advisable to start with

¹<https://www.mucar3.de/icra2024-continuous-clustering>

the most likely pairs, i.e., those from the same column or row [11]. Most of these approaches even only compare with points from the same [8] or additionally spatially close column (or row) [7], [10], [11] to reduce combinatorics.

Another possibility is to compare cluster metadata instead of individual points. For instance, [8] compares the spatial arrangement of the center of gravity of two clusters with each other. In fact, this is done already for the first one dimensional step to perform hierarchical agglomerative clustering over the entire column.

The aim of our approach, is similar to [10], to evaluate a rectangular FOV around each point. We make the FOV's size dependent on the distance of the current point. For closer points, a larger field of view is evaluated, such that even the challenging scenarios in Section IV are clustered correctly.

III. PROPOSED METHOD

In the following, each stage of our continuous clustering pipeline is described. The individual stages are designed to work in a pipelined fashion. This means that the stages can be parallelized while passing the job from one stage to the next. A horizontally continuous range image serves as the shared data structure. As the memory is limited, it is implemented as a cyclic buffer, which stores the last W columns in a queue and still allows random access to the individual cells. The height of the range image corresponds to the number of lasers of the LiDAR sensor: $H = 128$.

The first stage, described in Section III-A, inserts a firing into the continuous range image, visualized in Figure 1a. It also identifies potentially completed columns, which are passed on to the ground point segmentation stage, explained in Section III-B. Here, each point is classified as obstacle or ground point. In the next stage, these obstacle points of a column are aggregated and associated to point trees as described in Section III-C. Furthermore, these trees are linked to each other if they belong to the same cluster. In the final stage, explained in Section III-D, finished clusters are identified by analyzing all unpublished point trees.

A. Continuous Range Image Generation

A 2D range image drastically reduces the computational complexity in order to find neighbor points compared to an unordered point cloud. We use the concepts of [5]–[10], [12] and extend them to the continuous case.

The row index i_{row} of a point is equal to the laser diode index ordered by their elevation angle. Points generated by the laser diode with the highest elevation angle are inserted at the top row of the range image.

In our case the sensor is rotating clockwise, which means that new points are added to the right of the existing range image. A point's column index i_{col} is calculated based on its continuous azimuth angle φ_{cont} . It is defined as $\varphi_{\text{cont}} = (-\varphi + \pi) + 2\pi i_{\text{rot}}$, where i_{rot} is the rotation index, $\varphi = \text{atan2}(y, x)$, and (x, y, z) is the Cartesian position of the current point. This ensures, that φ_{cont} is monotonically increasing for a laser diode in a clockwise rotating sensor despite the opposite direction and the cyclic nature of atan2 .

This simplifies calculations in later processing steps. The rotation index of a point is typically the same as the rotation index of the rearmost laser: $i_{\text{rot}} = i_{\text{rot, rear}}$. However, if a firing intersects the discontinuity at the negative x -axis, points, which already passed it, use rotation index $i_{\text{rot}} = i_{\text{rot, rear}} + 1$. The rotation index of the rearmost laser $i_{\text{rot, rear}}$ starts with 0 and is incremented whenever the rearmost laser of a firing passes the negative x -axis.

The global column index of a point in the continuous range image is defined as $i_{\text{col}} = \lfloor \varphi_{\text{cont}} / \Delta\varphi_{\text{col}} \rfloor$, where $\Delta\varphi_{\text{col}} = 2\pi / N_{\text{firings}}$ is the angular column width and N_{firings} is a constant representing approximately the predicted number of firings per rotation. Our sensor approximately generates 1800 firings per rotation: $N_{\text{firings}} = 1800$. Since the global column index is always increasing, it has to be mapped to the local column index of the cyclic buffer storing the continuous range image. This step, however, is omitted in the following to keep the explanation simple.

The Cartesian position (x, y, z) of a point p is calculated as: $(x, y, z)^{\text{T}} = \mathbf{R}_t \cdot (x', y', z')^{\text{T}}$, where \mathbf{R}_t is the rotation matrix from sensor frame to a world fixed odometry frame at time t and (x', y', z') is the point's position in sensor frame. The reason to choose the position relative to the sensor in a world-fixed frame is that clustering as well as ground point segmentation are performed in this frame. So it is more natural to construct the range image based on these coordinates. Another advantage is that a particular number of columns represents a full rotation in a fixed frame no matter whether the ego robot has rotated. However, it is also possible to construct the range image based on sensor coordinates as the differences in the resulting range images are marginal. In some use cases sensor coordinates are even preferred, especially when the sensor is mounted on a rolling or pitching platform like the 2-DoF platform in [13].

Finally, all columns whose column index $i_{\text{col}} < i_{\text{col, rear}} = \lfloor \varphi_{\text{cont, rear}} / \Delta\varphi_{\text{col}} \rfloor$ are considered to be finished, where $i_{\text{col, rear}}$ and $\varphi_{\text{cont, rear}}$ are the global column index and the continuous azimuth angle of the current firing's rearmost laser, respectively.

B. Ground Point Classification

For ground point classification we use similar concepts to [12]. A column is processed from bottom to top as visualized in Figure 2a. Points inside the ego vehicle's bounding are omitted (magenta points). If the z coordinate of the first outside point matches the minimum of the ego robot, the point is classified as ground. Subsequent points are also labeled as ground if the previous point was a ground point and the slope (yellow line) is small enough. When calculating the slope it is beneficial to use the point's position in a world-fixed frame whose xy -plane is approximately aligned with the ground plane. In this frame a slope near zero still means a flat line even if the sensor is mounted with a downward pitch angle.

Since not all ground points are found with this strategy, the algorithm in [12] also searches for ground points in the rows of the range image. This is more challenging in our

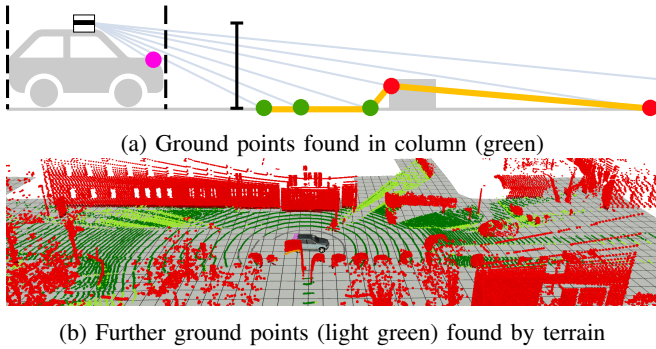


Fig. 2: **Ground Point Classification:** In the first pass (a) quite certain ground points are labeled based on the ego vehicle’s bounding box, the sensor’s height over ground and the slope between consecutive points in a column. In the second pass (b) remaining points are as labeled as ground, if their absolute z distance to the estimated terrain (gray) is below a threshold. The terrain estimation [14] gets the certain ground points (a) of the previous time steps as input.

case as only the current and previous columns are available. Therefore, we use a terrain estimation module as described in [14], which uses the certain ground points from the first pass for input. It accumulates these ground points over time and generates a world-fixed estimation of the terrain. This terrain is used to find remaining ground points based on the point’s z distance to this terrain. This is shown in Figure 2b.

C. Point Tree Construction

The main challenge for continuous clustering is the requirement to process the data in real-time. This holds for both, the regular clustering as well as the additional challenge to evaluate at a high frequency which clusters are completed and therefore are ready to be published.

We use a hierarchical data representation for this task visualized in Figure 3. More specifically, in this stage a undirected and potentially cyclic graph $G = (V, E)$ is generated, where each vertex $v \in V$ represents a set of points P_v . Each set of points P_v is stored as a point tree in the range image. The points $p \in P_v$ are required to belong to the same cluster but do not necessarily represent the whole cluster. Any point p from the entire point cloud P has to be associated to exactly one point tree and vertex v . The edges of the high-level graph G are generated such that:

$$E = \{\{v, v'\} \mid v, v' \in V \wedge \exists (p, p') \in P_v \times P_{v'} : \|\overrightarrow{pp'}\| < d_T\}.$$

In other words: two vertices (point trees) are linked if any of their points are closer than d_T . Such an edge is visualized in the second step of Figure 3 by an orange arrow.

For continuous clustering also a column-wise clustering in the first pass is a possible option. However, since the graph G is traversed at a high frequency in the subsequent stage for connected component labeling (CCL), it is important to keep the number of vertices $|V|$ and edges $|E|$ as small as possible. Therefore, we use point trees, which, in the best case, can represent the whole cluster. In other words it is a

minimum spanning tree of the cluster. In the scenario shown in the figure, two point trees are required due to the specific shape of the cluster, which is first vertically separated and merged in a later column.

In order to represent the point trees, each cell c in the range image contains a set of 2D indices $I_{\text{childs},c}$ pointing to its child cells. Due to the traversal of cells inside the field of view (FOV), the child cells c' are always below and/or to the right of the current cell c . It is important to traverse the whole FOV in order to ensure that the set E includes all required high-level edges, as visualized in step 2 in Figure 3. For this process it is required to know the existing tree ID for a potential parent cell (cyan and green color of cells). Therefore, we save for each cell the 2D index $i_{\text{root},v}$ of its tree’s root, which can be also used as tree identifier of the current cell. By using the high-level links $e \in E$ we can merge two trees without requiring to relabel $i_{\text{root},v}$ for all points within a tree.

For the subsequent processing stages it is sufficient to work with these aggregated points in form of G in order to perform further clustering and reasoning about cluster completion. However, additional point tree meta data is required for each vertex $v \in V$. In order to fully store graph G , it is sufficient to have a set of 2D range image indices pointing to the roots of all unpublished point trees I_{root} . The remaining data for a point tree is stored in the range image at the referenced cell. It includes $E_v \subseteq E$, which are the high-level edges outgoing from the current point tree. This set is extended whenever a point is found, which was already associated to a point tree and is close enough to a point of another point tree. In order to represent E_v it is sufficient to store the 2D range image index of the other point tree root. Furthermore, the cell includes $\varphi_{\text{finished},v}$, which represents the required continuous azimuth angle of a future firing’s rearmost laser $\varphi_{\text{cont, rear}}$ at which no more point can be added to the point tree as the angular difference is too large. It is updated whenever a point p is added to the tree and is calculated as $\max(\varphi_{\text{finished},v}, \varphi_p + \arcsin(d_T/r_p))$, where φ_p and r_p are the continuous azimuth angle and the radius of the added point and $\varphi_{\text{finished},v}$ is the previous earliest completion angle of point tree v . When the cluster is finally published, the individual points can be efficiently retrieved by traversing the point trees starting from their roots.

D. Cluster Generation

Since graph G contains very few nodes and edges, it is possible to perform a new run of connected component labeling (CCL) after each arrival of a new column i_{col} , which was already processed in the previous stages. Only minor extensions compared to existing approaches are necessary. Firstly, every node v , i.e., every point tree, must be finished. This is the case when the azimuth angle of the rearmost laser is far enough from the point tree: $\varphi_{\text{cont, rear}} > \varphi_{\text{finished},v}$. If a single incomplete node is found, the corresponding nodes are not removed from the graph. However, this traversal within the connected component is continued to the end in order to mark the remaining nodes as visited. To avoid having to

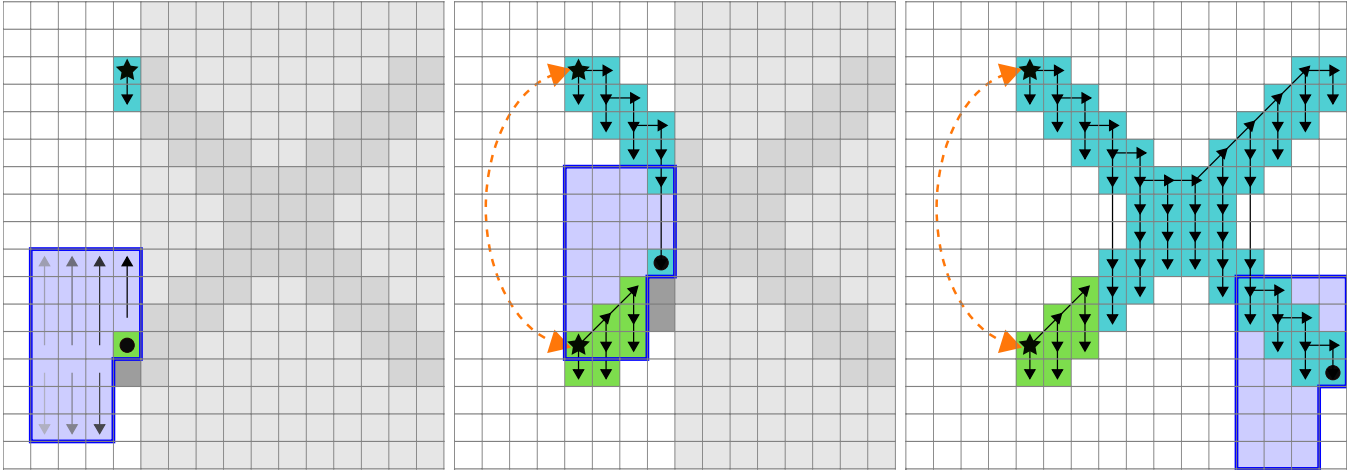


Fig. 3: **Clustering of a X-shaped object:** Each incoming column of the range image is processed from top to bottom. The required size of the field of view (FOV, blue area) for the current point p (black circle) is calculated such that it includes all neighbor points p' , which potentially could have a distance smaller than the distance threshold: $\|\vec{pp'}\| < d_T$. More specifically, all cells have to be evaluated whose angular difference to the current cell is smaller than $\arcsin(d_T/r_p)$, where r_p is the current point's radius w.r.t. sensor origin. The cells inside the FOV are evaluated as indicated by the arrows (from dark to bright). If no neighbor is found, the current point becomes the root of a new point tree (black star). Otherwise, it becomes the child (black arrow) of the neighbor found first. For the point in the second image, the FOV includes neighbors from different trees with distance below d_T . This means, that the point trees belong to the same cluster and therefore a mutual higher-level link (orange) is generated. This results in a high-level graph, where the vertices are point trees.

reset the visited flag each time, we instead use a continuously increasing value, for example, the global index of the latest column i_{col} . So it can be checked whether the node was already visited in the current run.

If a connected component with only complete nodes is found, these nodes are extracted from the graph, and their LiDAR points are assigned a single cluster ID and this cluster is published.

Finally, the algorithm iterates over the remaining point trees in I_{root} and the minimum column index is extracted. This is the minimum index which has to be kept in the ring buffer. All preceding columns are ready to be cleared as the trees can only grow to the bottom and to the right.

E. Heuristics for Real-Time Capability

The algorithm, as described in previous sections, delivers exact clustering results based on the Euclidean distance d_T . Despite many optimizations like the dynamic size of the FOV and efficient data structures, this version of the algorithm is not real-time capable. On our test system with a mid-range CPU, it is around 4 to 5 times too slow, depending on the average distance of points in the scene. The most computationally demanding step is iterating over the potentially large FOV for each obstacle point. Instead of limiting the FOV size, we use a different approach, which is explained in Figure 4. As a result, the point trees produced with this heuristic remain equivalent to the exact method. However, the high-level edges E_{approx} in G_{approx} might be incomplete, potentially affecting clustering. However, it is observed that two point trees belonging to the same object are still very likely to be combined through another node. Due to

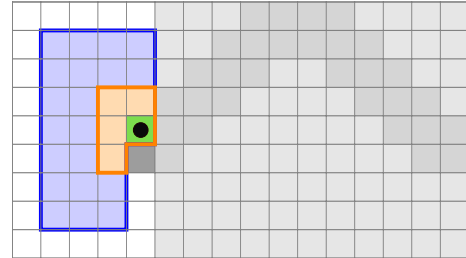


Fig. 4: **Heuristic A:** Instead of evaluating the full field of view (blue), only the yellow part with configurable size is completely evaluated. The outer blue part is only evaluated subsequently as long no neighbor was found. While the generated low level point trees are equivalent, the yellow area is important to generate a set of high-level edges, which is ideally as complete as in the exact solution.

this heuristic, the FOV search can often be terminated much earlier compared to the exact method, significantly reducing computational demand and making the approach real-time capable on average hardware.

If it is desired to further optimize the processing time, we found it beneficial to artificially halve the number of obstacle points. Instead of ignoring entire rows or columns, cells in the range image are skipped in a checkerboard pattern, as shown in Figure 5b.

IV. EVALUATION

The class-agnostic nature of distance-based clustering is both an advantage and a disadvantage. It facilitates the

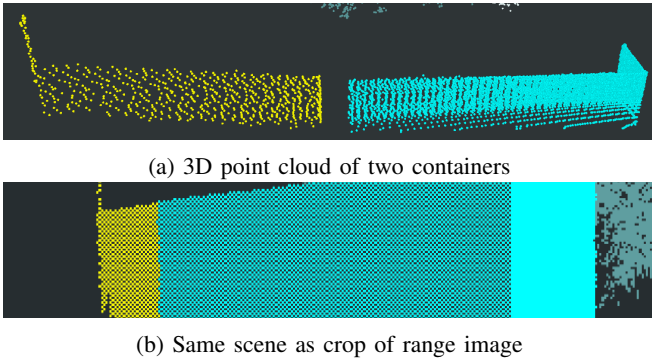


Fig. 5: **Heuristic B:** The yellow cluster and parts of the blue cluster are clustered only with cells distributed in a checkerboard pattern. At the right side of (b) this heuristic is disabled and the range image becomes dense. In (a), despite ignoring half of the points and the LiDAR sensor hitting the walls at a sharp angle, the points remain evenly spread without significant gaps. Ignoring entire columns in the range image would result in problematic gaps.

TABLE I: Quantitative analysis on SemanticKitti [17] using under- (USE) and over-segmentation entropy (OSE)

Approach	Metric		USE		OSE	
	$\mu \downarrow$	$\sigma \downarrow$	$\mu \downarrow$	$\sigma \downarrow$	$\mu \downarrow$	$\sigma \downarrow$
GPF + SLR [7]	117.08	127.40	301.16	144.29		
TRAVEL [11]	24.07	11.88	70.40	34.44		
Proposed (w/ Heur. A, RT)	23.74	11.21	65.79	25.52		
Proposed (exact, non-RT)	23.74	11.21	65.23	23.88		

detection of various object types; however, without additional processing, there’s no object classification available. This becomes particularly problematic when evaluating with established object detection benchmarks [15]–[18], as their metrics inherently rely on object classification. Therefore, in [11], the metrics over-segmentation entropy (OSE) and under-segmentation entropy (USE) were introduced in order to evaluate over-segmentation and under-segmentation, respectively, irrespective of the class. These metrics are evaluated using the SemanticKitti [17] dataset.

In Table I, our approach is compared to others based on these metrics. Furthermore, the implications of the heuristic A from Section III-E are presented. The distance threshold in our methods is set at $d_T = 0.7$. It’s evident that our approach, despite its low-latency nature, achieves superior segmentation. The precise but non-real-time approach yields the best results. However, the approach with heuristic A, which is an approximation but real-time capable on standard hardware, performs only slightly worse. Compared to other approaches [7], [11], the issue of over-segmentation is significantly mitigated by the enlarged perceptive field of view. However, the enlarged FOV doesn’t mitigate the under-segmentation problem. It can be observed that adding additional metrics, like considering convexity during graph edge formation, doesn’t substantially reduce under-segmentation in the SemanticKitti scenarios.

In Figure 6 a very challenging scenario is shown, due

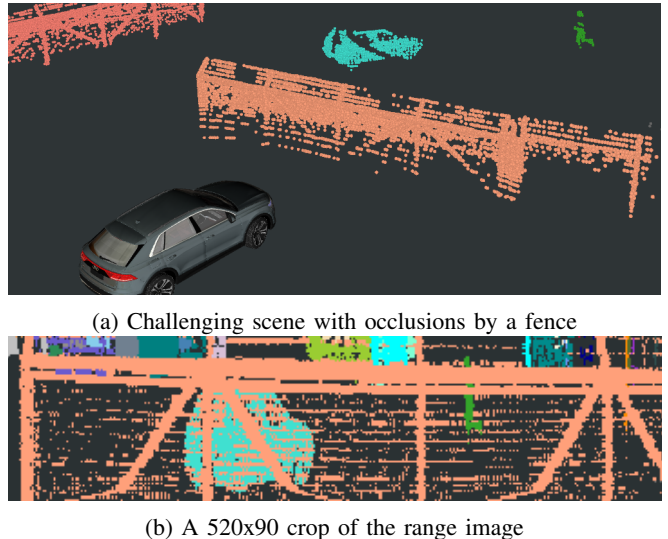


Fig. 6: **Importance of FOV:** In order to correctly segment the fence (orange), the car (cyan) and the pedestrian (green) in (a) a rectangular FOV of at least 10x9 is required in (b).

to heavy occlusions. It shows the importance of being able to use a large FOV when necessary. Some approaches use a 4-neighborhood for each grid cell [5], [6], which is very efficient. Hierarchical approaches [7]–[11] have a similar, but larger, cross-shaped FOV around the currently-evaluated cell, where the first dimension often has a larger field of view compared to the second. Most approaches have a field of view of only one cell in the second dimension for efficiency reasons. Due to the aforementioned cross shape, all these approaches have difficulties with oblique and sparse structures in the range image. Even seemingly straight obstacles, like a streetlamp, can have a horizontal jump in the depth image due to slight twists. The approach with the largest field of view is described in [10], which has a view distance of up to 3 cells in both dimensions and either direction. However, a scenario as shown in Figure 6 can only be handled correctly by our approach, which is able to use a very large FOV when required.

Our algorithm has an average latency of $\mu = 3$ ms with a standard deviation of $\sigma = 2$ ms. For a cluster’s reference timestamp, we utilize the timestamp of its most recent LiDAR point. Consequently, the integration time of the cluster, which depends on the angular size of the object, is already accounted for. This is useful for measuring how quickly finished clusters are detected, aggregated, and published.

V. CONCLUSIONS

In this study, we introduced an algorithm capable of clustering a continuous stream of LiDAR points in real time without prior accumulation. This significantly reduces the latency of individual object instances. Simultaneously, it allows for a much larger field of view compared to existing methods, considerably enhancing the results in challenging scenarios with occlusions.

REFERENCES

- [1] W. Han, Z. Zhang, *et al.*, “Streaming object detection for 3-d point clouds,” in *Proc. European Conf. Comput. Vision (ECCV)*, 2020.
- [2] Q. Chen, S. Vora, and O. Beijbom, “Polarstream: Streaming object detection and segmentation with polar pillars,” *Advances in Neural Information Processing Systems (NIPS)*, 2021.
- [3] R. Loiseau, M. Aubry, and L. Landrieu, “Online segmentation of lidar sequences: Dataset and algorithm,” in *Proc. European Conf. Comput. Vision (ECCV)*, 2022.
- [4] M. Abdelfattah, K. Yuan, Z. J. Wang, and R. Ward, “Multi-modal streaming 3d object detection,” *IEEE Robot. Autom. Lett.*, 2023.
- [5] F. Moosmann, O. Pink, and C. Stiller, “Segmentation of 3d lidar data in non-flat urban environments using a local convexity criterion,” in *Proc. IEEE Intelligent Vehicles Symp. (IV)*, 2009.
- [6] I. Bogoslavskyi and C. Stachniss, “Fast range image-based segmentation of sparse 3d laser scans for online operation,” in *Proc. IEEE/RSJ Int. Conf. Intelligent Robots and Syst. (IROS)*, 2016.
- [7] D. Zermas, I. Izzat, and N. Papanikolopoulos, “Fast segmentation of 3d point clouds: A paradigm on lidar data for autonomous vehicle applications,” in *Proc. IEEE Int. Conf. Robotics and Automation (ICRA)*, 2017.
- [8] P. Burger, B. Naujoks, and H.-J. Wuensche, “Fast Dual Decomposition based Mesh-Graph Clustering for Point Clouds,” in *Proc. IEEE Intelligent Transportation Syst. Conf. (ITSC)*, 2018.
- [9] H. Yang, Z. Wang, *et al.*, “Two-layer-graph clustering for real-time 3d lidar point cloud segmentation,” *Appl. Sci.*, 2020.
- [10] X. Zhang and X. Huang, “Real-time fast channel clustering for lidar point cloud,” *IEEE Trans. Circuits Syst. II*, 2022.
- [11] M. Oh, E. Jung, *et al.*, “Travel: Traversable ground and above-ground object segmentation using graph representation of 3d lidar scans,” *IEEE Robot. Autom. Lett.*, 2022.
- [12] A. Reich and H.-J. Wuensche, “Fast detection of moving traffic participants in lidar point clouds by using particles augmented with free space information,” in *Proc. IEEE/RSJ Int. Conf. Intelligent Robots and Syst. (IROS)*, 2022.
- [13] M. Karimi, M. Oelsch, *et al.*, “Lola-slam: Low-latency lidar slam using continuous scan slicing,” *IEEE Robot. Autom. Lett.*, 2021.
- [14] B. Forkel, J. Kallwies, and H.-J. Wuensche, “Probabilistic terrain estimation for autonomous off-road driving,” in *Proc. IEEE Int. Conf. Robotics and Automation (ICRA)*, 2021.
- [15] H. Caesar, V. Bankiti, *et al.*, “nuScenes: A Multimodal Dataset for Autonomous Driving,” in *Proc. IEEE Conf. Comput. Vision and Pattern Recognition (CVPR)*, 2020.
- [16] A. Geiger, P. Lenz, and R. Urtasun, “Are we ready for Autonomous Driving? The KITTI Vision Benchmark Suite,” in *Proc. IEEE Conf. Comput. Vision and Pattern Recognition (CVPR)*, 2012.
- [17] J. Behley, M. Garbade, *et al.*, “SemanticKITTI: A Dataset for Semantic Scene Understanding of LiDAR Sequences,” in *Proc. IEEE Int. Conf. Comput. Vision (ICCV)*, 2019.
- [18] P. Sun, H. Kretzschmar, *et al.*, “Scalability in Perception for Autonomous Driving: Waymo Open Dataset,” in *Proc. IEEE Conf. Comput. Vision and Pattern Recognition (CVPR)*, 2020.